Quantified Relation between Grain Boundary Angle and Interfacial Stability of PWA1484 Superalloy during Thermal Exposure

QINJIA WANG, JINXIA SONG, DINGGANG WANG, CHENGBO XIAO, and XIDONG HUI

Nowadays, the tolerance of grain boundaries (GBs) is a crucial subject of single crystal (SX) superalloys. Quantitatively deciphering the effect of GBs on the interfacial stability may provide theoretical guidance for the technological design and engineering application of SX superalloys. In this article, [001] tilt artificial GBs with grain boundary angles (GBAs) of 5, 15, 25, 35, and 45 deg, respectively, have been prepared by directional solidification for PAW1484 SX superalloy. The microstructural evolution at GBs under thermal exposure at 1070 °C up to 1000 hours was quantitatively investigated. It has been revealed that low-angle grain boundaries (LAGBs) (< 15 deg) maintained a straight and narrow interface and have no precipitates (mainly carbides) around GBs. For GBAs higher than 25 deg, however, the γ' layer was widened and coherent MC carbides with orientation relationships $[001]_{MC}//[001]_{matrix}$ and $\langle 001\rangle_{MC}//\langle 001\rangle_{matrix}$, together with blocky and closely spaced M_6C carbides, were precipitated. By carefully scaling, the width of the γ' layer and the ratio of carbides to the γ' layer were quantitatively determined as a function of GBAs and thermal exposure time. Furthermore, it has been confirmed that the topological-closed-packed (TCP) phase precipitated along the 45 deg GB with the increase of thermal exposure time.

https://doi.org/10.1007/s11661-019-05510-8

I. INTRODUCTION

NICKEL-BASED single crystal (SX) superalloys have excellent comprehensive properties, which makes them one of the main application materials of high-pressure turbine blades at present. The excellent mechanical properties of SX superalloys depend on the misfit of γ/γ', suitable volume fraction of γ' phase, γ channel width, and solution strengthening elements (such as Re, W, Mo, and Ta) in the matrix.[1,2] During thermal exposure, the microstructures of superalloys are mainly degraded by γ' coarsening, primary MC degeneration, precipitation, and evolution of secondary carbides within grain interiors, topological-closed-packed (TCP) phase formation,[3] and so forth. Previous works[4–6] have confirmed that some of these changes may cause deterioration of mechanical properties in SX superalloys. Therefore, microstructural stability at elevated temperatures has been a vital issue for superalloys.

From the traditionally cast superalloy to the SX superalloy, elimination of the GB plays a vital role. Grain boundary in the traditional sense is characterized by five degrees of freedom (DOF): three to characterize the three unique rotations from one lattice to the next and two more to distinguish the plane separating the two grains.[7] In terms of larger scale, the GB in SX can be determined as the misorientation between adjacent dendrites. The misorientation between the two sides of the GB is the main characteristic parameter that determines the structure and properties of superalloys. Elimination of GBs significantly increases creep resistance of SX superalloys. This has been demonstrated by experiments on the CMSX-4 superalloy,[8] which was designed to be used in SX form, *i.e.*, with no GBs present. The results showed that the stress rupture life of a perfect SX exceeded 10,000 hours, but the creep life is reduced to 100 hours for a GB of misorientation $\theta = 7$ deg and further drops to a few hours for that with $\theta > 10$ deg, under the condition of an applied stress

QINJIA WANG is with the State Key Laboratory for Advanced Metals and Materials, University of Science and Technology Beijing, Beijing 100083, China, and the Science and Technology on Advanced High Temperature Structural Materials Laboratory, AECC Beijing Institute of Aeronautical Materials, Beijing 100095, China. JINXIA SONG, DINGGANG WANG, and CHENGBO XIAO are with the Science and Technology on Advanced High Temperature Structural Materials Laboratory, AECC Beijing Institute of Aeronautical Materials. Contact email: songjx@vip.sina.com XIDONG HUI is with the State Key Laboratory for Advanced Metals and Materials, University of Science and Technology Beijing. Contact email: xdhui@ustb.edu.cn

Manuscript submitted February 18, 2019.
Article published online November 7, 2019

of 300 MPa at 850 °C. The sensitivity of creep life to the appearance of GBs is also found widely in Mar-M200[9] and René N4 SX superalloys.[10,11] Moreover, misorientation of the GB has been reported to significantly affect the tensile strength in DD6 and CMSX-10K. When the GBA exceeds 9 deg (at 800 °C to 1000 °C)[12] and 12 deg (at 899 °C),[13] respectively, the tensile properties deteriorate significantly.

From an engineering point of view, the complex blade structure, temperature field, and solute field are intertwined during the directional solidification of SX blades, and it is inevitable to form casting defects such as freckles,[14,15] stray grain,[16,17] sliver defects,[18] and GBs.[2,19–21] These defects will have a harmful influence on the properties of SX castings and even directly lead to scrapping. Therefore, research on defects has attracted much attention in the materials fields. Compared with other defects, GB defects, especially low-angle grain boundaries (LAGBs), are relatively less studied. In the process of using the SX superalloy blade, because the principal stress direction of the blade is approximately parallel to the interface direction of the LAGB, the effect of the LAGB is negligible on the longitudinal properties of the blade. Meanwhile, considering the economy and viability of casting production, LAGBs to a certain extent are allowed, which is also known as grain boundary (GB) tolerance. In general, the tolerance value of LAGBs is 6 deg, such as Rene N SX superalloy[22] and CM186LC SX superalloy.[23] As the components and process conditions differ from one to another, some SX superalloys, for example, PWA1483 superalloy,[24] may be allowed to have tolerance up to 10 deg. It is noted that the evolution of the microstructures at GBs is still unclear, although SX superalloys with tolerable LAGBs might possess backscatter mechanical properties. Hence, GBs should be paid more attention for SX superalloys during the process of thermal exposure.

On the other hand, the evolution of carbides is also related to the GB of SX superalloys. Carbides at GBs often pin down dislocation movement and inhibit GB migration during deformation, thus enhancing the fatigue performance of superalloys.[11,25] However, continuous carbide chains formed at GBs would facilitate the initiation and propagation of cracks, resulting in failure of superalloys.[26] During thermal exposure, the size of carbides increases, which is detrimental to the adhesion of GBs.

The stability and precipitation behavior of GBs with different grain boundary angles (GBAs) can vary significantly. High GB energy and diffusion mobility of refractory alloying elements may transform the γ-γ' two-phase microstructure into γ-γ' + TCP lamellar structure. Nystrom *et al.*[3] reported that cellular discontinuous precipitation occurred at GBs with misorientation higher than 10 deg at 1093 °C in a bicrystal superalloy containing 6.7 wt pct Re. Yu *et al.*[27] suggested that cellular structure exists along the 25 deg GBs of SX superalloy containing 5 wt pct Re after heat treatment at 1100 °C for 50 hours. Huang *et al.*[28] found that the TCP phase precipitated at 10 deg GB of DD6 SX superalloy even without thermal exposure. This further increases the difficulty of improving GB tolerances.

PWA1484 is a second-generation Ni-based SX superalloy that is widely used in many jet engines as the high-pressure turbine blades for both military and commercial applications. Nevertheless, quantitative correlation of the GBA to the interfacial stability has not been reported until now. Therefore, in order to better understand the microstructural evolution of GBs in the PWA1484 superalloy, interfacial stability under standard heat treatment and the long-term thermal exposure condition was quantitatively studied through the characterization of γ' phase and GB precipitates (carbides or TCP phase). The present work may provide the foundation for evaluating the tolerance of the GBA of PWA1484 SX superalloy in future work.

II. MATERIAL AND EXPERIMENTAL PROCEDURE

The nominal composition of second-generation Ni-based SX superalloy PWA1484 used in this study is given in Table I. The bicrystal slabs of 120 × 75 × 15 mm in dimension with GBAs of 5, 15, 25, 35, and 45 deg, respectively, were prepared with double-seed molds, achieved by rotating one of the [001] seeds in the (001) plane.

Figure 1 is a schematic of the bicrystal slab. While fixing the [010] and [100] directions of one seed crystal parallel to the width and lengthwise directions of the slab, respectively, the other seed was rotated around its [001] axis to achieve the desired GBAs. Bicrystal slabs were directionally solidified by the conventional Bridgman casting technique with the withdrawal rate of 3 mm/min. The crystal orientation of the slabs was determined with Laue XRD and the GBA was calculated.

The bicrystal slabs with different GBAs were standard heat treated and the standard heat treatment regime is as follows: 1315 °C/4 h/AC + 1079 °C/4 h/AC + 704 °C/24 h/AC. Then the samples were subjected to long-term thermal exposure for 200, 400, 600, 800, and 1000 hours under the temperature of 1070 °C without applied stress. We chose 1070 °C for the following two reasons. From the perspective of operating temperature, the entire operating temperature range of the PWA1484 superalloy is below 1100 °C. Sometimes part of the blades may reach 1070 °C in the operation process. On the other hand, this temperature is also within the limits of the precipitation temperature of TCP phases. So, this temperature can fully demonstrate the microstructural stability of PWA1484 superalloy at high temperature. The samples for observation were cut normal to the [001] primary growth direction by the wire cutting machine. The samples were first mechanically polished and then chemically etched in an electrolyte solution containing 5 g of $CuSO_4$, 20 mL of HCl, and 25 mL of distilled H_2O. Scanning electron microscopy (SEM) and backscattered electron imaging mode observations were conducted using a ZEISS AURIGA field-emission scanning electron microscope. Energy-dispersive X-ray

Table I. Nominal Composition of PWA1484 Alloy (Weight Percent)

Alloy	Ni	Co	Cr	Mo	W	Ta	Re
PWA1484	bal	10	5	2	6	9	3
Alloy	Hf	Al	C	B	Si	S	P
PWA1484	0.1	5.6	< 0.02	< 0.001	< 0.10	< 0.001	< 0.005

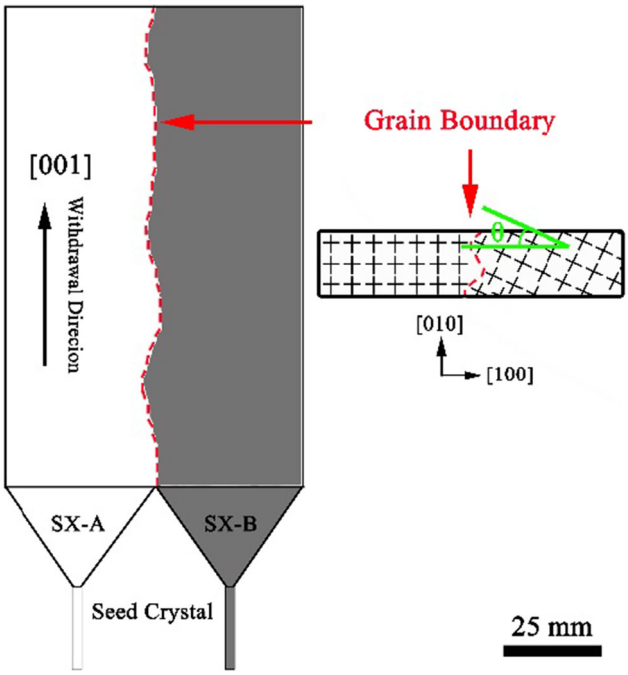

Fig. 1—Schematic diagram of the bicrystal.

spectroscopy (EDS) analysis was performed to ascertain compositions of phases using an Oxford LINK ISIS system attached to the ZEISS AURIGA field-emission scanning electron microscope. The evolution of the GB microstructure is quantitatively characterized as the width of the γ' layer, which is defined by the width perpendicular to the GB growth direction. In one graph, the width of 12 equalized positions is measured. The ratio of carbides to the γ' layer is another characteristic quantity, which is defined by the $A_c/A_{\gamma'}$ ratio, where Ac is the area of carbides. To obtain statistically significant results, 12 images were used in each sample. Transmission electron microscopy (TEM) analysis was performed for the specimens after standard heat treatment and thermal exposure. The specimens for TEM study were first mechanically ground to ~ 30 μm in thickness followed by twin-jet electrochemical polishing using an electrolyte solution containing 10 pct perchloric acid and 90 pct ethanol at − 20 °C. The TEM observation was conducted using a FEI Technic-T20. TEM thin foils of Re-rich phase along the 45 deg GB after thermal exposure at 1070 °C for 1000 hours were prepared using a ZEISS AURIGA Dual Beam (FIB/SEM) workstation.

III. RESULTS AND DISCUSSION

A. *As-Cast Microstructures*

The representative microstructure of the as-cast alloy with a high-angle grain boundary (HAGB) of 45 deg is shown in Figure 2. Figure 2(a) presents a typical cross-sectional optical image, in which the black dashed line indicates the location of the GB of bicrystal. The matrix is mainly composed of irregular γ' phase and narrow γ channel. The primary carbides and (γ + γ') eutectics, which usually form during casting, are found in interdendritic regions (Figure 2(b)). Some of these carbides are associated with eutectic edges, and some exist alone. The EDX analyses confirm that the carbides (rich in Ta and Hf elements) are of MC type. In addition, it is difficult to distinguish the exact position of the LAGB because of the similarity of the two sides of the bicrystal.

B. *Microstructures after Standard Heat Treatment*

Figure 3 shows the SEM micrographs of the microstructure around GB regions after standard heat treatment. After this process, the microstructure of the matrix consists of cuboidal γ' phase and thin γ phase channels. The (γ + γ') eutectics in the interdendritic regions are almost dissolved, and the volume fraction of residual (γ + γ') eutectic is less than 0.5 pct.

The effect of the GBA on the microstructure can be observed in Figure 3. As shown in Figure 3(a), bicrystals with an LAGB of 5 deg integrate well through the tightly aligned γ' phase. However, some abnormally coarsened γ' phases begin to appear along the 25 deg GB (Figure 3(b)). The difference in microstructures at 45 deg GB is more obvious. In Figure 3(c), coarse γ' phases (indicated by the red arrow) at GBs become much more prominent and the γ' phase adjacent to the GB shows some extent of coalescence; thus, the γ phase was eliminated from the GB. The average width of the γ' layer at GBs is remarkably increased to 2 μm, which gives more space and the elemental condition for the precipitation.

These microstructures indicate that the proportion of the γ phase at GBs decreases with the increase of GBA, whereas the proportion of γ' phase increases. In addition, coarse γ' phases formed when the GBA is high and both the size and quantity of coarse γ' phase increase with increasing GBA.

The presence of carbides at GBs is another critical phenomenon. It is seen that the size and quantity of carbides increase obviously with increasing GBA. In Figure 3(a), minimal carbides were found along the GB

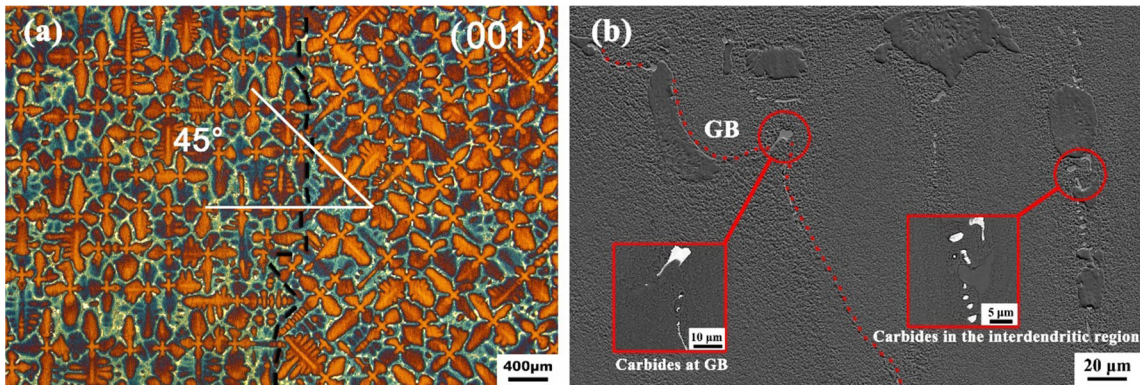

Fig. 2—Microstructures of as-cast sample with 45 deg GB: (*a*) optical of GB region and (*b*) SEM image of GB region.

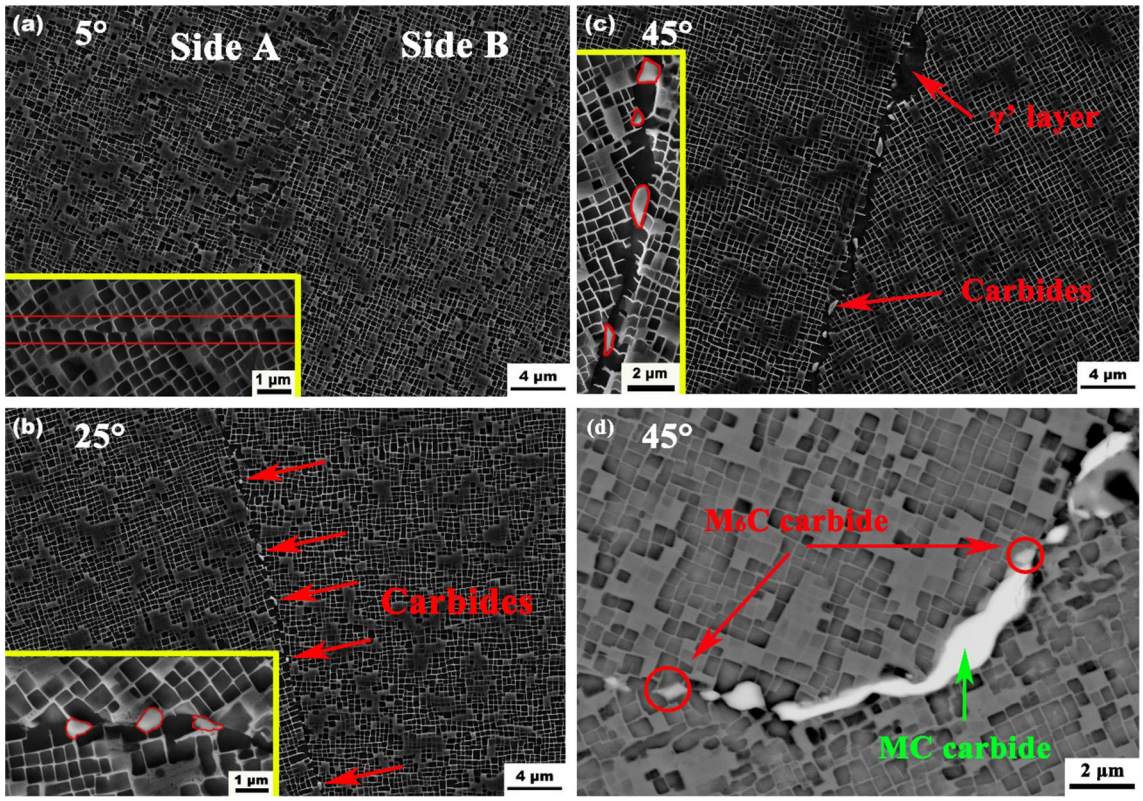

Fig. 3—SEM images of GB microstructures in bicrystals with (*a*) 5 deg, (*b*) 25 deg, and (*c*) 45 deg. (*d*) Backscatter electron images of 45 deg GB. The [001] direction of these samples is perpendicular to the paper surface.

and only small and discontinuous carbides were observed along the 25 deg GB (Figure 3(b)), while for a HAGB of 45 deg, many more carbides appeared at the GB. The size of carbides at the 25 deg GB was < 0.5 μm. These particles are enriched with Ta and Hf elements, as were the bigger granules at the 45 deg GB. However, the smaller granules mainly consist of strengthening elements of W, Mo, and Re at the 45 deg GB.

From Figures 3(a) through (c), it is seen that both the size and quantity of carbides increase obviously with increasing GBA, and these carbides are enriched with Ta and Hf elements. In order to gain insight into the details of these carbides, we further magnified the microstructure at 45 deg GB (Figure 3(d)). The carbides, which are enriched with W, Mo, and Re elements (indicated by a red circle), were observed in some local regions along the GB, and their sizes are much smaller than those of the main carbide (bright contrast).

Further detailed information about carbides at GBs was investigated by TEM. As shown in Figure 4, the crystal structures of GB carbides were resolved by a series of selected-area electron diffraction (SAED) images, and here, we only show one set of images. The main carbide at the 45 deg GB was identified as MC carbide with a face-centered-cubic (fcc) type of structure

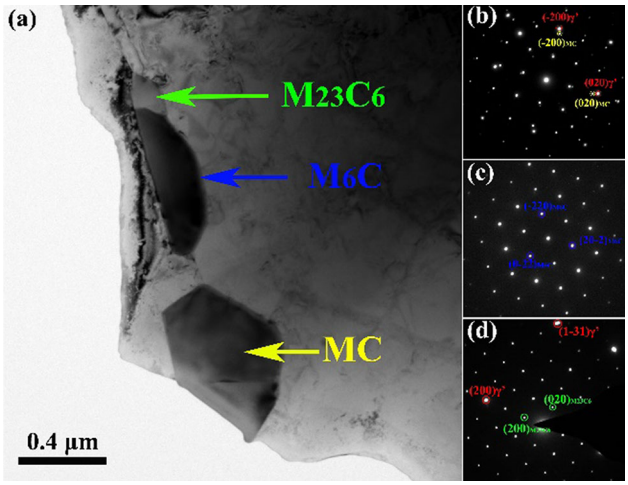

Fig. 4—(*a*) TEM micrograph of the GB of a sample in the standard heat treatment state. Three types of carbides decorate the GB. The SAED images show (*b*) MC carbide, (*c*) M_6C carbide, and (*d*) $M_{23}C_6$ carbide.

and lattice constant of $a = 0.399$ nm, as shown in Figure 4(b). The results indicated that the MC carbide has orientation relationships of $[001]_{MC}//[001]_{matrix}$ and $<001>_{MC}$ // $<001>_{matrix}$, with one side of the grains at the GB, which is the same as the case in previous research works.[29,30] Meanwhile, in Figure 4(c), the gray-contrast carbide in the backscatter electron image was identified as M_6C carbide (fcc, $a = 1.110$ nm) and no preferred orientation relationship was observed. Besides the two kinds of carbide mentioned previously, we have also found a very small amount of $M_{23}C_6$ carbide (fcc, $a = 1.064$ nm) grown next to M_6C carbide (Figure 4(d)). No preferred crystallographic orientation relationship was observed between $M_{23}C_6$ carbide and matrix yet. Although $M_{23}C_6$ carbides were observed in the TEM image, their sizes are not large enough to distinguish in SEM images. According to our extensive observation, the M_6C and $M_{23}C_6$ carbides precipitated alone at GBs in the form of fine granular during heat treatment.

C. *Microstructural Evolution During the Thermal Exposure*

The typical microstructures near GBs with GBAs of 5, 25, and 45 deg after heat treatment at 1070 °C for 200 to 1000 hours are given in Figure 5. It is seen that starting from the standard heat-treated condition, the γ' phase in the matrix gradually exhibited normal coarsening behavior until exposure for 1000 hours. A few TCP phases appeared at the matrix region, as shown in Figure 5(j), which is similar to the literature results.[31–34]

In the case of 5 deg GB, the morphology of the GB remains straight and the two grains seem to be combined through almost continuous bright-contrast γ phase. Carbides are scarcely found until 1000 hours. Then, with the increase of the BA, the initial γ' layer under standard heat treatment begins to widen obviously, as shown in Figures 5(d) through (i). At the same time, carbides are observed at the GB and these particles even form a straight chain in dispersion with the prolongation of exposure time, while for the GB of 45 deg, the microstructural evolution is more obvious and different from those of the LAGB and mid-HAGB. The discontinuous and slender γ phase, which is perpendicular to the extension direction of the GB, is found at GB channels. Short-chain carbide grew into a continuous belt structure and occupied most of the γ' layer at 600 hours. When thermal exposure time reached 1000 hours, the belt structured carbides decreased and the discontinuous precipitation reaction occurred, which contained a three-phase cellular structure: a continuous γ' matrix, disordered γ lamellae, and Re-rich phase. The composition of Re-rich phase is given in Table III. In view of the obvious difference in Re content between the M_6C carbide and Re-rich phase, TEM samples were prepared using FIB liftouts from the 45 deg GB. Figure 6 shows the presence of Re-rich phase, which was identified as the orthorhombic P phase, with lattice parameters of $a = 1.727$ nm, $b = 0.481$ nm, and $c = 0.914$ nm. According to the preceding observation, the microstructures of GBs with different angles under thermal exposure at 1070 °C have been carefully investigated mainly in two aspects: γ' configuration and carbides at GB. Here, we show microstructural evolutions of GBs under all conditions in Table II.

1. *γ' layer broadening*

The width of the γ' layer is measured and plotted as a function of thermal exposure time in Figure 7(a). The width of the γ' layer structure grows with increments of exposure time. The evolution can be divided into three types according to the trend of the curve. In the case of LAGBs (< 15 deg), the growth rate of the γ' layer is slow due to the good matching of two grains on both sides of the GB. Second, in the mid-HAGBs (15 to 25 deg), although the γ' layer is widened, the growth rate of the γ' layer remains stable with the prolongation of thermal exposure time. Further, in HAGBs (higher than 35 deg), the γ' layer grows smoothly during the preceding period, like that for mid-HAGBs, while dramatic growth of the γ' layer occurs after 800 hours.

The behaviors of the GBs with different GBAs stated previously are believed to be related to the atomic arrangement between neighboring grains and GB energy.[35] A quantitative description was put forward by Bulatov[36] for anisotropy of interfacial energy, which was also found to be universal for the crystallography class of fcc metals. According to Reference 36, GB energy continues to rise in the range of 0 to 45 deg, in spite of a slight drop near 38 deg. The peak energy appears near 45 deg. Hence, in our study, misorientation is the main factor affecting the morphology of the γ' layer. Moreover, atoms at LAGBs match well, resulting in an extremely low mobility.[37] Reference [38] shows that for GBs with a [001] axis of rotation, GB mobility is only maintained at a relatively low level in the range of 0 to 10 deg but increases rapidly in the range of 10 to 20 deg in Al, which also has the same fcc structure as nickel-based SX superalloy. This is similar to the results

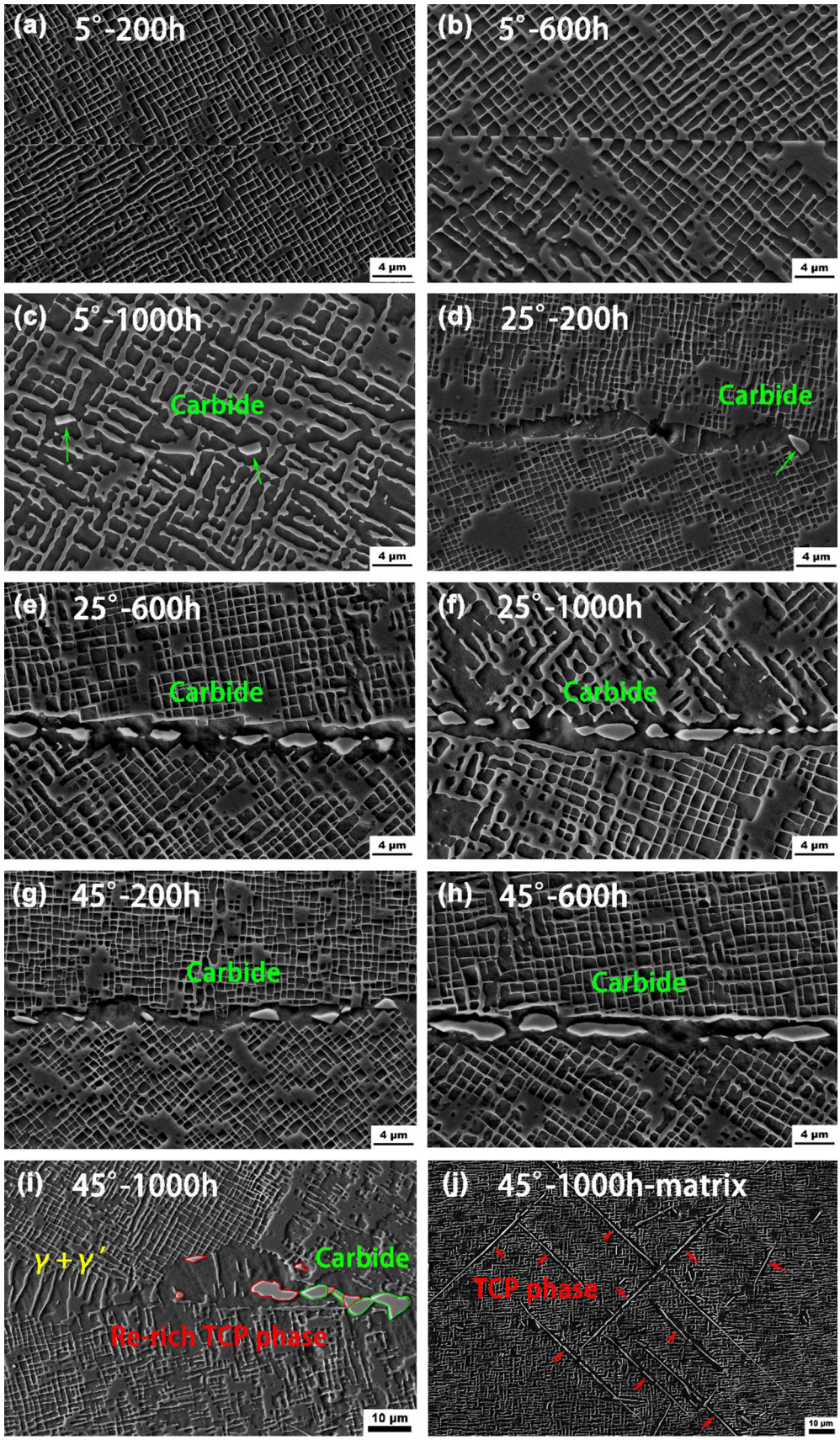
(a) 5°-200h
4 μm
(b) 5°-600h
4 μm
(c) 5°-1000h
Carbide
4 μm
(d) 25°-200h
Carbide
4 μm
(e) 25°-600h
Carbide
4 μm
(f) 25°-1000h
Carbide
4 μm
(g) 45°-200h
Carbide
4 μm
(h) 45°-600h
Carbide
4 μm
(i) 45°-1000h
γ+γ'
Carbide
Re-rich TCP phase
10 μm
(j) 45°-1000h-matrix
TCP phase
10 μm

◀Fig. 5—Typical microstructures near GBs with different angles after heat treatment at 1070 °C for 200 to 1000 h. The [001] direction of these samples is perpendicular to the paper surface: (*a*) 5 deg, 200 h; (*b*) 5 deg, 600 h; (*c*) 5 deg, 1000 h; (*d*) 25 deg, 200 h; (*e*)25 deg, 600 h; (*f*) 25 deg, 1000 h; (*g*) 45 deg, 200 h; (*h*) 45 deg, 600 h; (*i*) 45 deg, 1000 h; and (*j*) 45 deg, 1000 h, matrix.

obtained in this work. It is seen that when the GBA exceeds 25 deg, the mobility of the GB is further accelerated. For GBs with higher angles, especially 45 deg, initial abnormal morphology of the GB may have been formed after solution treatment. The occurrence of coarse γ' layer accompanying the formation of serrations has been reported to be strongly dependent on heat treatment parameters, which include a higher homogenizing temperature as well as a larger cooling rate and cooling range.[39–41] Then, in subsequent heat treatment and exposure processes, GBs have sufficient time to grow. It is worth noting that the amplitude of serrations has also proved to increase with the GBAs.[41,42] This is one of the reasons why a 45 deg GB is more abnormal than other angles. Moreover, the GB as a short-circuit path can make the solute rapidly reach an equilibrium state. Thus, in order to establish a more stable equilibrium state, a discontinuous precipitation reaction occurs, as shown by heterogeneous precipitation of γ' layers and carbides accompanying the formation of serrations at the moving GB.[43,44] It has also been suggested[45] that alloy composition plays a role, for instance, by providing a driving force for GB serrations from discontinuous element segregation along GBs. It is well known that C, as a strong segregation element at GBs, even combines with a large number of refractory elements to form carbides at GBs. If the strain energy generated by these carbides accumulates and results in the deformation of the GB itself, it can be inferred that the serration GB may be caused by discontinuous segregation.

2. *Evolution of carbides at the GBs*

The ratio of precipitates to the γ' layer in GBs as a function of thermal exposure time is shown in Figure 7(b), where precipitates here stands for all kinds of carbides presented in GBs. Especially, for the 45 deg GB, it is inevitable that the TCP phases, which are difficult to distinguish only from morphology, were added to the statistics of precipitates. As mentioned earlier, the low GB energy and mobility at LAGBs make it difficult to nucleate and grow precipitates. Therefore, the morphology of LAGBs remains stable. For HAGBs, the number and size of carbides at the GB in the initial stage are small. These precipitates are mainly carbides formed after standard heat treatment. Meanwhile, the γ' layer grew quickly due to the effect of GB energy. All these changes lead to a decrease in the ratio. With the prolongation of time, effective elements of carbide precipitation are continuously absorbed by GBs during growth and the migration of GBs to the matrix, providing sufficient kinetic and thermodynamic conditions for the precipitation of new carbides. At the same time, the initial carbides coarsen. So, the ratio is gradually rising. As time further increases, the degradation reaction of initial carbides becomes more and more obvious, which means that the size of the primary carbide (MC carbide) does not change much and more γ' phases precipitate simultaneously. Hence, the ratio decreases again after 600 hours.

In short, the evolution of carbides at GBs with the rise of the GBA or exposure time go through the following processes: (1) primary MC particles and small discrete

Table II. Microstructural Evolutions at GBs

Condition	MC	M_6C	$M_{23}C_6$	γ' Layer	TCP
As-Cast					
LAGB	×	×	×	×	×
HAGB	√	—	—	×	×
Standard Heat Treatment					
LAGB	×	×	×	×	×
mid-HAGB	√	√	—	×	×
HAGB	√	√	√	√	×
Thermal Exposure at 1070 °C					
LAGB	×	×	×	×	×
mid-HAGB	√	√	—	√	×
HAGB	√	√	—	√	√

"—" represents not sure.

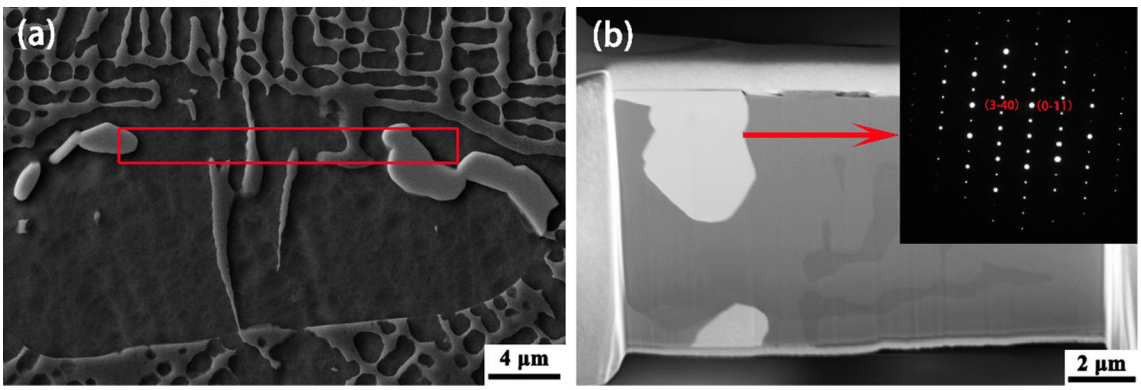

Fig. 6—(*a*) SEM image of Re-rich P phase at the 45 deg GB after thermal exposure at 1070 °C for 1000 h. (*b*) FIB liftout thin film of the area marked in the red rectangle in (a); the inset corresponds to the SAED of the bright phase taken from the $[433]_p$ zone axis.

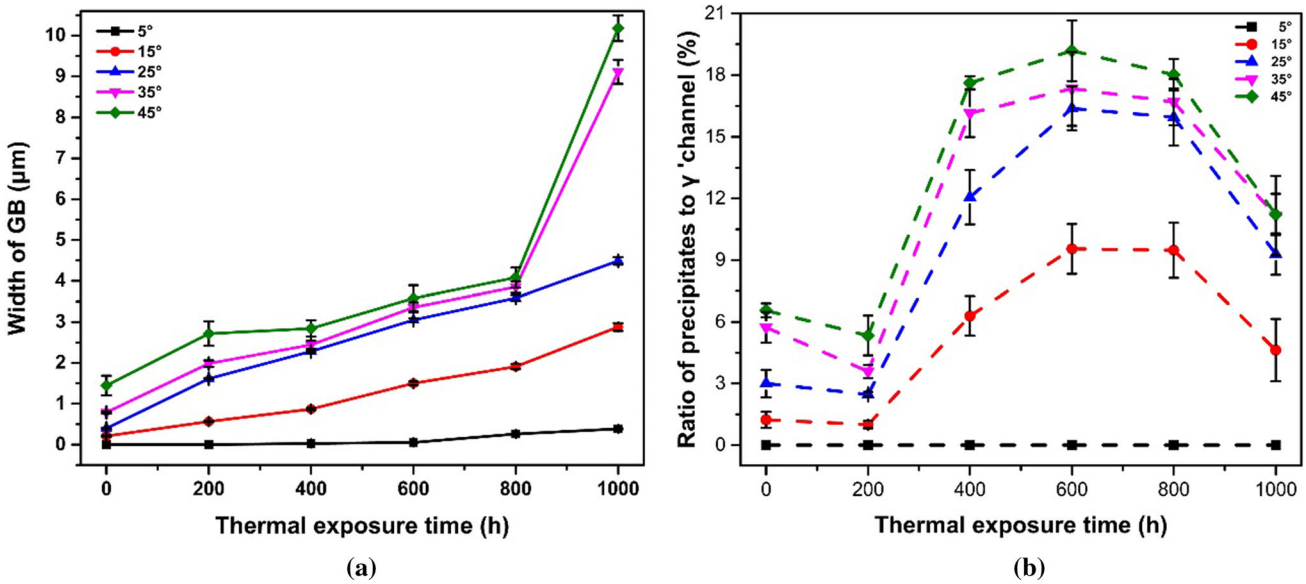

Fig. 7—(*a*) Average widths of γ' layer boundaries and (*b*) the ratio of precipitates to the γ' layer as a function of exposure time after heat treatment at 1070 °C.

M_6C carbides, which formed by an autonomous precipitation or degradation reaction at GBs, grow and gradually interlink into a thin discontinuous chain and then a coarse continuous chain; (2) a continuous γ' layer forms on either side of the chain and becomes thicker.

The structure of M_6C carbides was further investigated by TEM in detail. As shown in Figure 8, the combined SAED analysis confirmed that M_6C carbides are of fcc structure with the lattice parameter of a = 1.081 nm. The amount and size of M_6C carbides increased with the increment of thermal exposure time. Taking 45 deg samples as an example, the sizes of M_6C carbide grew from < 1 μm in the standard heat treatment state to 2 to 4 μm after exposure of 1000 hours. Two different morphologies of MC carbide formed at GBs during casting: irregular and discontinuous bulk type formed at corners and nodule type consisting of continuous small particles (Figure 2(b)). After standard heat treatment, nodule-type MC carbides disappear, leaving only random dispersed small particles, which may grow or decompose during subsequent thermal exposure. Moreover, during thermal exposure, block-type (4 to 10 μm) MC carbides are hard to find at GBs. It is well established that MC carbide has degenerated into M_6C carbide, as shown in Figure 9. The W and Mo-rich carbides (M_6C-type) formed both near and on the surfaces of some MC carbides. With the prolongation of time, more and more MC carbides were consumed and replaced by M_6C carbides (Figure 9). This phenomenon was observed more frequently in HAGBs. The decomposition of MC carbide takes place according to the following reaction: MC + $\gamma \rightarrow M_6C + \gamma'$, a reaction widely reported in the literature.[5,46,47]

To reveal the concentration of the alloying elements of these carbides, EDS analysis was performed, and the results are given in Table III. It is found that M_6C carbides are enriched in refractory elements W and Mo

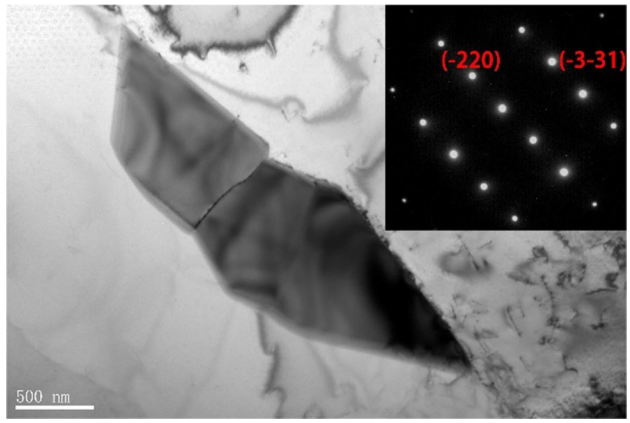

Fig. 8—TEM image of carbide at the 45 deg GB after thermal exposure at 1070 °C for 1000 h and the corresponding SAED $[116]_{M6C}$.

and also contain a large amount of Cr and Re elements. The content of Cr in the M_6C carbide precipitated after thermal exposure obviously increased when compared with that after standard heat treatment. It is also noted that $M_{23}C_6$ carbides were not found in the specimens after thermal exposure. Dong *et al.*[48] believe that the formation of $M_{23}C_6$ at the tips of M_6C particles (Figure 4) can be attributed to the local gradual accumulation of Cr. During the growth of M_6C in subsequent thermal exposures, C interstitially diffuses much faster than Cr migrates[30] so that Cr remains in the M_6C carbide rather than nucleating $M_{23}C_6$ carbide at the edge or inside the M_6C carbide. Meanwhile, it must be admitted that Cr concentration plays an important role in the stability of M_6C carbide. The M_6C carbides decompose into $M_{23}C_6$ carbide from 800 °C to 1000 °C, and the growth rate of $M_{23}C_6$

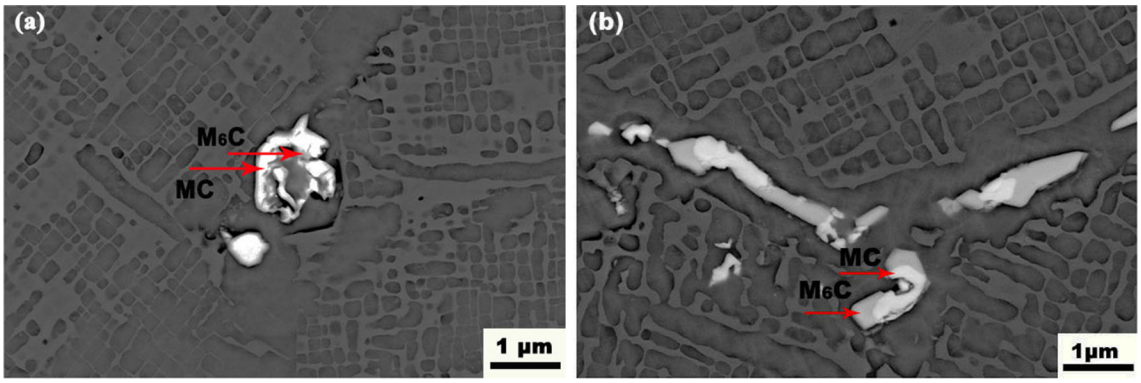

Fig. 9—Backscatter electron images of the 45 deg samples after heat treatment at 1070 °C for (*a*) 200 h and (*b*) 1000 h. The [001] direction of these samples is perpendicular to the paper surface.

Table III. Compositions of Several Precipitates in Three States (Atomic Percent)

	Ta	Cr	Re	W	Mo	Ni + Co + Al
M_6C (Standard Heat Treatment)	7.45	9.40	4.04	11.10	11.31	bal
M_6C (Exposure for 200 h)	6.91	14.83	5.49	18.51	14.79	bal
M_6C (Exposure for 1000 h)	3.96	18.49	7.2	15.01	14.2	bal
Re-rich TCP Phase (Exposure for 1000 h)	0.35	15.33	22.39	12.99	9.18	bal

carbide is dependent on both exposure temperature and time.[49] However, the decomposition reaction of the M_6C carbide above 1000 °C needs further study.

IV. CONCLUSIONS

In the present study, the microstructural stability under thermal exposure with different GBAs and exposure times was investigated for the second-generation Ni-based SX superalloy PWA1484. The conclusions can be summarized as follows.

1. Bicrystals with a LAGB of 5 deg integrate well through tightly aligned γ' phase. For GBAs > 15 deg, the higher the GBA, the wider the γ' layer in the GB and the greater the number of carbides precipitated in the γ' layer under standard heat treatment.
2. Under long-term thermal exposure at 1070 °C, the microstructure and interface can remain stable at a GBA of 5 deg, while for the HAGB, the γ' layer at GBs was broadened and the number of carbides at GBs was sharply increased. The width of the γ' layer and the ratio of carbides to the γ' layer can be quantitatively determined as a function of GBAs and thermal exposure times.
3. One of the main carbides at the 45 deg GB is MC carbide with orientation relationships $[001]_{MC}$ // $[001]_{matrix}$ and $<001>_{MC}$ // $<001>_{matrix}$. The degradation reaction was mainly originated from MC carbides to M_6C carbides.
4. The TCP phase was found along the 45 deg GB at 1070 °C for 1000 hours.

ACKNOWLEDGMENTS

This work was financially supported by the National Key Research and Development Program of China (Grant No. 2016YFB0701402), Aeronautical Science Foundation of China (Grant No. 2015ZE21006), National Natural Science Foundation of China (Grant No. 51771020) and the Foundation of Science and Technology on Advanced High Temperature Structural Materials Laboratory, AECC Beijing Institute of Aeronautical Materials, China (Grant No. 6142903190101).

REFERENCES

1. J.-B. Le Graverend, J. Cormier, and F. Gallerneau: *Int. J. Plastic.*, 2014, vol. 59, pp. 55–83.
2. R.C. Reed: *The Superalloys: Fundamentals and Applications*, Cambridge University Press, Cambridge, 2008.
3. J.D. Nystrom, T.M. Pollock, W.H. Murphy, and A. Garg: *Metall. Mater. Trans. A*, 1997, vol. 28A, pp. 2443–52.
4. G. Lvov, V. Levit, and M. Kaufman: *Metall. Mater. Trans. A*, 2004, vol. 35A, pp. 1669–79.
5. Q. Chen, N. Jones, and D. Knowles: *Acta Mater.*, 2002, vol. 50, pp. 1095–12.
6. W. Sha: *Scr. Mater.*, 2000, vol. 42, pp. 549–53.
7. M.D. Sangid, H. Sehitoglu, and T. Niendorf: *Mater. Sci. Eng.: A*, 2010, vol. 527, pp. 7115–25.
8. P. Lukáš, J. Čadek, and L. Kunz: *Kovove Mater.*, 2005, vol. 43, pp. 5–19.
9. B. Kear and B. Piearcey: *AIME Trans.*, 1967, vol. 239, pp. 1209–15.
10. J.C. Stinville, K. Gallup, and T.M. Pollock: *Metall. Mater. Trans. A*, 2015, vol. 46A, pp. 2516–29.
11. Q. Chen, C. Jones, and D. Knowles: *Mater. Sci. Eng.: A*, 2004, vol. 385, pp. 402–18.
12. Y. Patel, P.F. Browning, and M.D. Fitzpatrick: *ASME Turbo Expo*, 2000, p. V004T01A005.

13. J. Li, J. Zhao, S. Liu, and M. Han: *Superalloys*, TMS, Warrendale, PA, 2008, pp. 443–51.
14. S. Tin, T.M. Pollock, and W. Murphy: *Metall. Mater. Trans. A*, 2001, vol. 32A, pp. 1743–53.
15. Q. Li, J. Shen, and L. Qin: *J. Alloys Compd.*, 2016, vol. 691, pp. 997–1004.
16. M.M. Ter Vehn: *Superalloys*, TMS, Warrendale, PA, 1966, p. 471.
17. X. Yang, H. Dong, and W. Wang: *Mater. Sci. Eng. A*, 2004, vol. 386, pp. 129–39.
18. J.W. Aveson, P.A. Tennant, and B.J. Foss: *Acta Mater.*, 2013, vol. 61, pp. 5162–71.
19. M. Newell, N. D'Souza, and N.R. Green: *Mater. Sci. Eng. A*, 2005, vol. 413, p. 67.
20. W. Bogdanowicz, R. Albrecht, and J. Sieniawski: *J. Cryst. Growth*, 2014, vol. 401, pp. 418–22.
21. T.M. Pollock and S. Tin: *J. Propul. Power*, 2006, vol. 22, pp. 361–74.
22. E.W. Ross and K.S. O'Hara: *Superalloys*, TMS, Warrendale, PA, 1996, pp. 19–25.
23. K. Harris and J.B. Wahl: *Superalloys*, TMS, Warrendale, PA, 2004, pp. 45–52.
24. D.M. Shah and A. Cetel: *Superalloys*, TMS, Warrendale, PA, 2000, pp. 295–304.
25. L. He, Q. Zheng, and A. Tieu: *Mater. Sci. Eng.: A*, 2005, vol. 397, pp. 297–304.
26. A. Koul and R. Castillo: *Metall. Trans. A*, 1988, vol. 19, pp. 2049–66.
27. Z. Yu, Y. Zheng, and Q. Feng: *Scr. Mater.*, 2017, vol. 128, pp. 23–26.
28. M. Huang, L. Zhuo, and J. Li: *Mater. Sci. Eng.: A*, 2015, vol. 640, pp. 394–401.
29. W. Sun, X. Qin, and L. Zhou: *Mater. Des.*, 2015, vol. 69, pp. 81–88.
30. X.Z. Qin, J.T. Guo, and H.Q. Ye: *Mater. Sci. Eng.: A*, 2008, vol. 485, pp. 74–79.
31. W. Zhixun, P. Haiqing, and Y. Zhufeng: *Rare Met. Mater. Eng.*, 2015, vol. 44, pp. 1873–78.
32. S. Gao, Y. Zhou, and T. Jin: *J. Alloys Compd.*, 2014, vol. 610, pp. 589–93.
33. B. Dubiel, R. Kalemba, and S. Kąc: *Mater. Charact.*, 2017, vol. 131, pp. 266–76.
34. B. Dubiel, P. Indyka, and A. Radziszewska: *J. Alloys Compd.*, 2018, vol. 731, pp. 693–703.
35. I. Manna, S. Pabi, and W. Gust: *Int. Mater. Rev.*, 2001, vol. 46, pp. 53–591.
36. V.V. Bulatov, B.W. Reed, and M. Kumar: *Acta Mater.*, 2014, vol. 65, pp. 161–75.
37. D.L. Olmsted, E.A. Holm, and S.M. Foiles: *Acta Mater.*, 2009, vol. 57, pp. 3704–13.
38. M.D. Sangid, T. Ezaz, and I.M. Robertson: *Acta Mater.*, 2011, vol. 59, pp. 283–96.
39. R.J. Mitchell, H.Y. Li, and Z.W. Huang: *J. Mater. Process. Technol.*, 2009, vol. 209, pp. 1011–17.
40. P. Kontis, E. Alabort, and D. Barba: *Acta Mater.*, 2017, vol. 124, pp. 489–500.
41. H.L. Danflou, M. Macia, and T. Khan: *Superalloys*, TMS, Warrendale, PA, 1996, pp. 119–27.
42. L. Jiang, R. Hu, and H. Fu: *Mater. Sci. Eng.: A*, 2012, vol. 536, pp. 37–44.
43. I. Kaur and W. Gust: in *Fundamentals of Grain and Interphase Boundary Diffusion*, I. Kaur and W. Gust, eds., Ziegler Press, Stuttgart, 1989, 2nd ed..
44. Y.S. Lim, D.J. Kim, and S.W. Kim: *Mater. Charact.*, 2014, vol. 96, pp. 28–39.
45. H.U. Hong, H.W. Jeong, and I.S. Kim: *Phil. Mag.*, 2012, vol. 92, pp. 2809–25.
46. C.T. Sims: *Superalloys II*, Wiley, New York, 1987, p. 1.
47. Y. Jinxia, Z. Qi, and H. Zhuangqi: *J. Mater. Sci.*, 2006, vol. 41, pp. 6476–78.
48. X. Dong, X. Zhang, and K. Du: *J. Mater. Sci. Technol.*, 2012, vol. 28, pp. 1031–38.
49. G. Bai, J. Li, and R. Hu: *Mater. Sci. Eng.: A*, 2011, vol. 528, pp. 2339–44.